EM and system-level modelling of phased antenna arrays for D-band antenna-in-package and antenna-on-package implementation at 150 GHz

Tengiz Svimonishvili, Mihai D. Rotaru
Institute of Microelectronics (IME), Agency for Science, Technology and Research (A*STAR)
2 Fusionopolis Way, Innovis #08-02, Singapore 138634, Republic of Singapore
svimonishv@ime.a-star.edu.sg

Abstract

The demand for higher data throughput in wireless communication has led to exploration of the D-band (110-170 GHz) due to its potential for near-100 Gb/s data rates. High-gain antennas and beamforming transceivers are essential for overcoming challenges such as high propagation losses and low output power at these frequencies. Phased antenna arrays, particularly those based on compact patch antennas, show promise for 6G wireless technologies. However, comprehensive system-level modeling for large N-by-N arrays in this frequency range is lacking. This paper presents an innovative approach merging electromagnetic (EM) and system-level modeling to analyze N-by-N phased antenna arrays ($3 \leq N \leq 20$) at 150 GHz. The modeling process is detailed, encompassing the design of a 150 GHz patch antenna and array synthesis in HFSS, followed by system-level simulations in SystemVue. The impact of beam steering on directivity and beamwidth is explored, both with and without phase quantization. Additionally, the effect of antenna element failure on directivity is investigated for 5-by-5 and 16-by-16 arrays, highlighting the significance of array size in performance resilience. The power consumption implications of array size are discussed, emphasizing the benefits of larger arrays in achieving a given system gain with fewer amplifiers. Finally, sidelobe level reduction is explored using Taylor tapering, resulting in decreased directivity and increased beamwidth, with specific trade-offs analyzed for different array sizes and steering angles.

Introduction

The evolution of wireless communication underscores the demand for higher data throughput, driven by data-intensive applications. In this context, the D-band (110-170 GHz) offers substantial advantages, with ample aggregate bandwidth and potential for efficient, integrated systems achieving nearly 100 Gb/s data rates. Nonetheless, challenges like high free-space propagation losses, low output power, and poor noise figure at THz frequencies necessitate high-gain antennas and beamforming transceivers. Array antennas enable precise electronic beamforming, improving signal quality, coverage, capacity, and efficiency. Specifically, antenna arrays based on compact and low-profile patch antenna designs are ideal for Antenna-on-Package (AoP) and antenna-in-package (AiP) implementations and have been central to ongoing research for future wireless 6G technologies [1].

The authors in [2] introduce a wideband circularly-polarized AiP element using Fan-Out Wafer-Level Packaging (FOWLP) technology for satellite communications. The AiP element employs a meta-surface radiator with an aperture-coupled feeding structure and achieves an impressive performance with a return Loss > 17.95 dB, axial ratio < 2.67 dB, and gain of 7.19 - 7.88 dBi over the frequency range of 27 to 31 GHz. The design is validated using printed circuit board (PCB) technology for rapid prototyping and evaluation, demonstrating wide bandwidth and desirable circular polarization patterns. In [3], a cost-effective and high-performance packaging solution is introduced for the D-band. The setup connects to an 8-element series-fed patch antenna on the carrier and exhibits a 11dB gain, a 12-degree E-plane 3-dB beamwidth, and a 6-GHz 3-dB bandwidth. The study in [4] presents a glass-based package for D-Band RF modules, integrating an 8-element patch antenna. Simulation results indicate that the integrated antenna array achieves a peak gain of 14.2 dBi at 141 GHz. Based on the findings it is claimed that the glass-based packaging solution exhibits substantial potential for facilitating the integration of RF modules in the D-Band. The work presented in [5] involves designing and simulating single antenna elements such as patch antennas, sub-arrays of patch antennas, and horn antennas at 26 GHz from the standpoint of minimizing power consumption while maintaining system performance and adhering to regulatory radiation standards in 5G backhaul networks. The array size is determined based on the required system gain and the output power of each power amplifier. In [6], the focus is on developing integrated packaging solutions for high-frequency antennas in the D-band for 6G wireless communication. The study showcases 4-element linear and 4-by-4 2-D rectangular patch antenna arrays on glass substrates, operating at around 140 GHz and achieving gains of up to a gain of 10.6 dBi and 16.2 dBi, respectively with reasonable bandwidth. The work presented in [7] discusses advancements in packaging and antenna integration for silicon-based millimeter-wave phased arrays, covering sub-100 GHz arrays, integration techniques, and upcoming challenges with an emphasis on the importance of integrating antenna arrays and RFICs in packaging for 5G and future 6G systems. In [8], the authors discuss the development of a 1-by-5 series-fed patch antenna array for 6G D-Band MIMO applications using FOWLP. The array's design, simulation, and fabrication at 140 GHz are detailed, along with the application of amplitude tapering to minimize sidelobe levels.

Currently, no comprehensive system-level modelling exists for large N-by-N antenna arrays in the 110-170 GHz D-Band range. Therefore, this paper introduces a novel method that merges electromagnetic (EM) and system-level modeling to assess N-by-N phased antenna arrays with sizes ranging from N = 3 to N = 20 at 150 GHz. The focus is on high-transmit antenna arrays utilizing compact patch antennas, making them well-suited for AoP and AiP applications. These antenna arrays are positioned as strong candidates for advancing wireless 6G technologies and are currently the central focus of extensive academic research.

The paper is organized as follows. The first section discusses the modeling methodology in HFSS and SystemVue. Subsequent three sections focus on beam steering with and without phase quantization and on the impact of beam steering on the realized gain and beamwidth of N-by-N antenna arrays. The next three sections discuss the impact of array antenna element failure on directivity, array size and associated power consumption implications, and the reduction of sidelobe levels using the Taylor taper. The penultimate section provides a general discussion of the results, whereas the last section is devoted to conclusions.

EM and system-level simulation methodology

The objective is to model and characterize a phased antenna array in the transmit mode for 6G applications at 150 GHz via EM and system-level simulations using HFSS (full-wave 3-D EM simulation software by Ansys) and SystemVue (system-level design software by PathWave System Design). The simulation methodology is divided into three distinct steps: 1) Simulating a simple patch antenna in HFSS that resonates at 150 GHz; 2) Synthesizing a uniform rectangular N-by-N array in HFSS such that N ranges from 3 to 20 and adjacent elements are spaced λ/2 apart at 150 GHz; 3) Using N-by-N arrays synthesized in HFSS to set up system-level simulations in SystemVue.

The initial modeling step involves forming a microstrip-fed copper patch antenna in HFSS that resonates at f_r = 150 GHz. The patch sits above a ground plain on a square Rogers RT/duroid 5880 substrate whose height, h, is 20 μm and whose side is 1 mm, which is equal to λ/2 at 150 GHz. The dielectric constant, ε_r, and tangent loss, δ, of the substrate are 2.2 and 0.0009, respectively. The actual length, L, and width, W, of the patch are calculated using the following formulas [9]:

$$W = \frac{c}{2f_r}\sqrt{\frac{2}{\varepsilon_r + 1}} \approx 664\ \mu m$$

$$L = \frac{1}{2f_r\sqrt{\varepsilon_{reff}\varepsilon_0\mu_0}} - 2\Delta L \approx 790\ \mu m$$

where c is the free-space velocity of light, ε_{reff} is the effective dielectric constant of the patch, ε_0 and μ_0 are the free-space permittivity and permeability, and ΔL is the extended incremental length of the patch. W and L in equations are further adjusted in HFSS to 652 μm and 842 μm, respectively, to obtain a patch antenna whose resonant frequency is at 150 GHz. The optimized patch antenna with its 3-D realized gain and return loss are shown in Fig. 1.

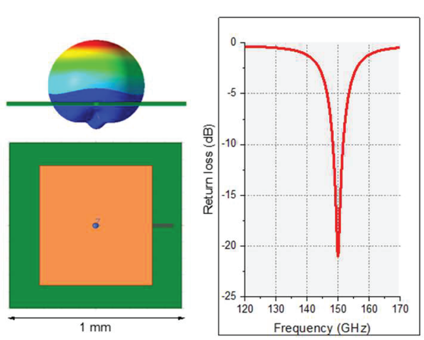

Fig. 1. Optimized patch antenna with an overlaid radiation pattern (left) and the variation of its return loss with frequency (right)

In Fig. 1, the image on the left shows the optimized microstrip-fed patch antenna and its typical unidirectional radiation pattern with a realized gain of about 3.5 dB. The return loss shown on the right is plotted over the frequency range of 120 to 170 GHz and exhibits a sharp minimum at 150 GHz. The patch antenna in Fig. 1 has a relatively narrow 10-dB bandwidth of approximately 2.3%.

After completing the first modeling step, the antenna in Fig. 1 is used as a unit cell in HFSS to create a uniform rectangular N-by-N array, where N ranges from 3 to 20 and the spacing between adjacent elements is λ/2 at 150 GHz. The array synthesis involves assigning coupled lattice pair boundaries to parallel planes (planes of periodicity) coincident with the patch antenna substrate edges where the E-field on the secondary boundary surface (at every point) is forced to match that on the primary boundary surface to within a phase difference. The coupled lattice pair boundaries are shown in Figs. 2a and 2b.

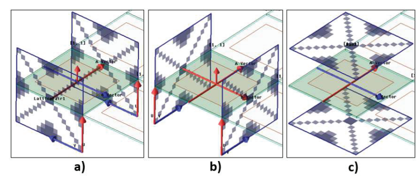

Fig. 2. Patch antenna as a unit cell for N-by-N array synthesis with coupled lattice pair boundaries in a) and b) and radiation boundary in c)

Figs. 2a and 2b show the coupled lattice pair boundaries assigned to faces coincident with the patch antenna substrate edges parallel to the z-x and z-y planes. Also shown in Fig. 2c is a radiation boundary assigned to faces parallel to the patch antenna and the x-y plane, at least λ/4 away from the radiating patch, for absorbing outgoing EM radiation. The unit cell so formed is subsequently duplicated along the x and y axes to produce a rectangular array of desired size as shown in Fig. 3a for a 5-by-5 rectangular array.

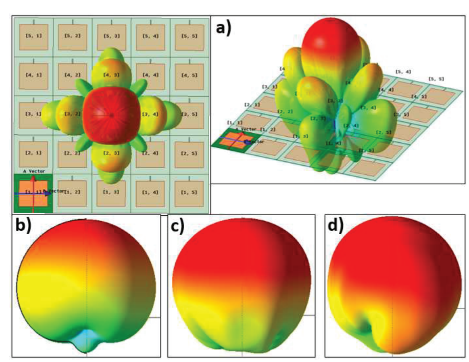

Fig. 3. a) 5-by-5 rectangular array synthesized by duplicating the patch antenna in Fig. 1 along the x and y axes; b) Far-field

pattern for an isolated patch antenna; c) and d) Far-field patterns for [2,2] and [5,5] elements in the 5-by-5 array

Fig. 3a represents top and isometric views of a 5-by-5 rectangular array and its far-field radiation patterns with characteristic main, side, and back lobes. The numbers in square brackets denote row and column indices, respectively. Note that the arrays thus formed in HFSS account for mutual antenna element coupling, which is significant for elements spaced λ/2 apart. Proximity effects between array elements can affect the radiation pattern and, consequently, directivity and gain. The effect of mutual coupling between two elements of 5-by-5 array in Fig. 3a is illustrated in Figs. 3b through 3d, where the patterns of [2,2] and [5,5] elements in Figs. 3c and 3d vary with their position and markedly deviate from that of the isolated patch antenna in Fig. 3b.

After completing the synthesis of N-by-N arrays and their subsequent EM simulations in HFSS, the final modeling step involves setting up system-level simulations using SystemVue. To accomplish this, radiation patterns (total realized gain) of sequentially excited elements of each of the simulated N-by-N arrays are exported to SystemVue and mapped to a planar grid with an equal spacing of d = λ/2 between adjacent elements. Figs. 4a through 4d outline the sequence of steps for a 3-by-3 antenna array and Fig. 5 compares directivity plots for 3-by-3, 5-by-5, 10-by-10, and 16-by-16 arrays simulated and extracted from HFSS and SystemVue.

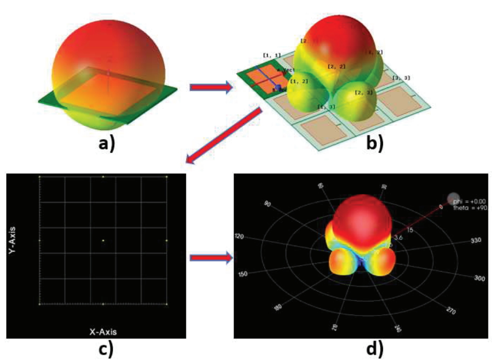

Fig. 4. a) Simulation of a single patch antenna resonating at 150 GHz using HFSS; b) Synthesis and simulation of a 3-by-3 antenna array derived from the single patch antenna in HFSS; c) SystemVue grid with λ/2 spacing for mapping sequentially excited 3-by-3 antenna array elements from HFSS; d) Visualization of the far-field radiation pattern for the 3-by-3 antenna array in SystemVue

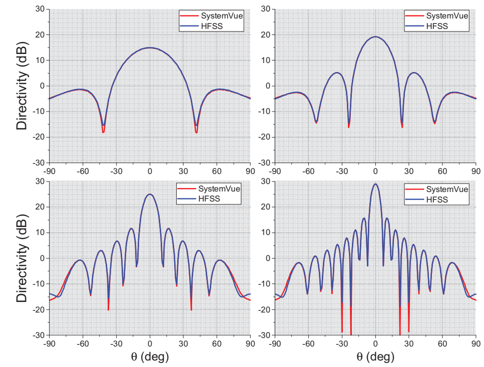

Fig. 5. Directivity as a function of zenith angle, θ, in ϕ = 0° plane for 3-by-3 (top left), 5-by-5 (top right), 10-by-10 (bottom left) and 16-by-16 (bottom right) arrays

As can be seen in Figs. 4b, 4d and 5, there is a strong correlation between both 3-D far-field patterns and 2-D directivity plots, where the red and blue curves in Fig. 5 correspond to SystemVue and HFSS, respectively. Each N-by-N array modeled in HFSS and subsequently mapped to a planar grid in SystemVue serves as a transmit antenna for system-level modeling in the schematic shown in Fig. 6, where each array element is part of a branch consisting of the attenuator, phase shifter, and amplifier. The branches are fed by a common source whose output signal is split into an N-by-N subarray and supplied to N attenuators, which can be used to control sidelobe levels, and N phase shifter by means of which the antenna array can be steered electronically by controlling the relative phases of the array elements. The amplifiers are inserted in the branch to compensate for losses incurred by the signals in going from the source to the antenna array elements.

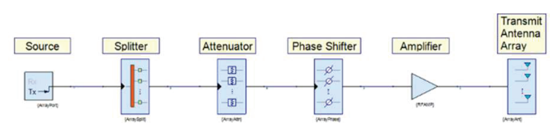

Fig. 6. Phased array architecture in SystemVue for combined EM and system-level modeling at 150 GHz

Beam steering in the absence of phase quantization

One of the main advantages of phased antenna arrays is their ability to steer the antenna beam. Although planar arrays can scan the main beam in any direction of θ (elevation) and ϕ (azimuth), we treat the case of beam steering in the ϕ = 0° elevation plane. For N-by-N patch antenna arrays considered here, this involves steering the beam from broadside at θ = 0° to some $\theta = \theta_{max}$ angle by the application of a linear phase distribution across the array. This is illustrated in Fig. 7 for the 5-by-5 array from Fig. 3a

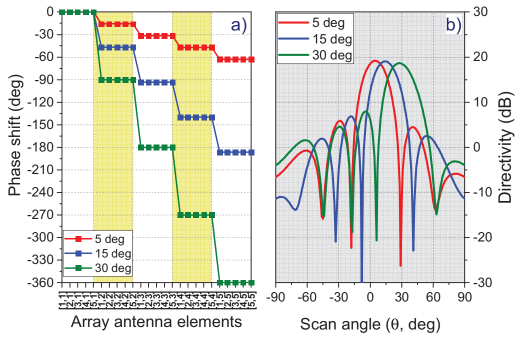

Fig. 7. a) Phase shifts applied to 5-by-5 array elements to steer the array to 5° (red), 15° (blue), and 30° (green); b) Directivity of 5-by-5 patch array antenna steered to 5° (red), 15° (blue), and 30° (green)

As can be seen in Fig. 7a, through the application of an incremental phase delay across the array, relative to elements [1,1] through [5,1] (Fig. 3a), the direction of maximum radiation can be steered to 5°, 15°, and 30° in the $\phi = 0°$ elevation plane (Fig. 7b). Note that the incremental phase delay required gets larger with increasing scan angle. Fig. 7 is plotted under the assumption of continuous phase. The effect of phase quantization on directivity is explored in one of the subsequent sections. The phase shifts that need to be applied to the individual signals in Fig. 7a are calculated by the phase shifter model in Fig. 6. Specifically, the phase adjustments are computed to align the resultant beam with the direction specified by the boresight zenith angle, θ, of the array. In addition, the array configuration and size play a significant role in influencing the computation of necessary phase adjustments.

Fig. 8 shows the variation of directivity (on a linear scale) with the zenith angle, θ, for 3-by-3, 7-by-7, 12-by-12, and 20-by-20 patch antenna arrays whose far-field patterns are steered to 15°, 30°, 45°, and 60°.

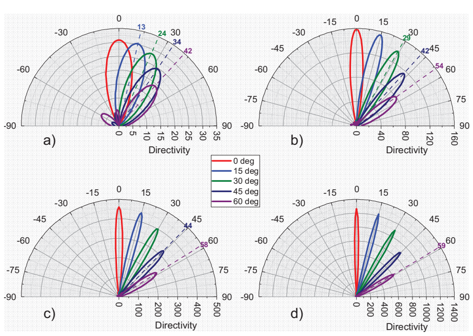

Fig. 8. Far-field patterns steered to 15° (blue), 30° (green), 45° (navy), and 60° (purple) in $\phi = 0°$ plane for a) 3-by-3, b) 7-by-7, c) 12-by-12, and d) 20-by-20 patch antenna arrays

As can be seen in Figs. 8a through 8d, θ_{max} (denoted by colored labels) to which the main lobe can be steered is influenced by the size of the array and mutual coupling among neighboring elements that are spaced at half-wavelength intervals. Specifically, the smaller the array, the more pronounced the influence and the smaller is the angle to which the main lobe can be steered. Consequently, when the 3-by-3 array is steered to 15°, 30°, 45°, and 60°, the main beam maxima occur at 13°, 24°, 34°, and 42° angles (Fig. 8a). The 7-by-7 array shown in Fig. 8b performs better in that its main beam maxima occur at 15°, 29°, 42°, and 54° when the array is steered to 15°, 30°, 45°, and 60°. Among the four arrays shown in Fig. 8, the largest 20-by-20 array demonstrates the best performance. As can be seen in Fig. 8d, its θ_{max} for the main beam aligns with angles of 15°, 30°, 45°, and 59° corresponding to steering angles of 15°, 30°, 45°, and 60°.

The impact of beam steering on realized gain and beamwidth

We observe in Figs. 8a through 8d that both the peak directivity (hence gain) and main lobe beamwidth are dependent on the steering angle. The variation of peak realized gain and main lobe beamwidth with steering angle for N-by-N arrays is explored next. The realized gain accounts for an antenna array efficiency besides its directional capabilities, whereas the main lobe beamwidth represents a 3-dB beamwidth, which is the full width of the main lobe at the half-power level. Fig. 9 displays the peak realized gain (left) and 3-dB beamwidth (right) in the elevation plane ($\phi = 0°$) for 9 different N-by-N arrays, when the arrays are steered to 15°, 30°, 45°, and 60°.

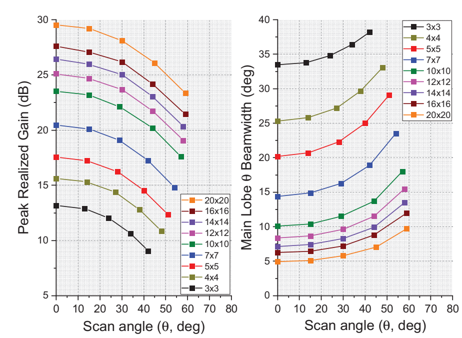

Fig. 9. Variation of peak realized gain (left) and main lobe θ beamwidth at half-power (right) with zenith angle, θ, in $\phi = 0°$ plane

Due to the size of the array (the number of elements making up the array) and mutual coupling between adjacent array elements, the usable scan angle θ to which the array can be steered is limited. Therefore, as can be seen in the left plot of Fig. 9, the main lobes for the smallest and largest arrays are steered to 42° and 60°, respectively. It can be observed that the smaller the array, the faster the peak value of realized gain drops with increasing θ. In Fig. 9, the peak realized gains for 3-by-3 and 20-by-20 arrays decrease by about 30% and 21%, respectively, as θ varies from 0° to 60°.

We can see in the right plot of Fig. 9 that the beamwidth increases with scanning angle regardless of the array size. Unlike the peak realized gain, however, the smaller the array, the slower is the rate with which the 3-dB beamwidth increases. Consequently, the percent increase in beamwidth is 23% and as much as 50% for 3-by-3 and 20-by-20 arrays, respectively, as θ varies over the range of 0 to 60°.

Beam steering in the presence of phase quantization

The simulations and discussion of beam steering in the previous two sections assume the absence of phase quantization for the phase shifter model in Fig. 6. In this section, we explore the impact of phase quantization on the directivity of the 5-by-5 array (Fig. 7) when its pattern is steered to 5°, 15°, and 30°. The quantization of the phase shifter values is performed using a uniform scheme with a specified number of bits. The process involves applying quantization to the phase shifter values, determined by the parameter NumBits, where NumBits indicates the bit count for quantization and determines the number of quantized levels, which is equal to 2^{NumBits}. Our analysis covers three scenarios: NumBits set to 4, 5, and 6, which correspond to 16, 32, and 64 quantized phase shift values, respectively. These values are uniformly distributed across the range of 0 to 360°.

Figs. 10a and 10b show the phase shift variation across antenna elements and the variation of directivity with the scan angle when the 5-by-5 array is steered to 5°. The cases of no quantization and NumBits = 4, 5, and 6 are displayed by the red, blue, green, and navy curves, respectively.

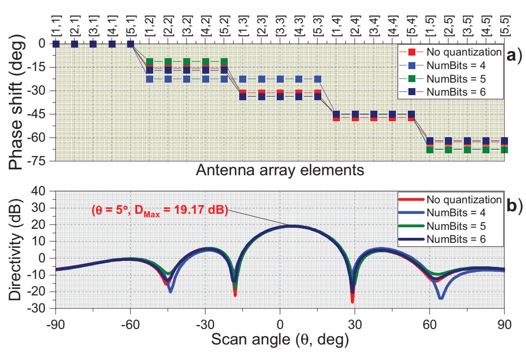

Fig. 10. a) Phase shift values without (red) and with (blue, green, navy) phase quantization applied to 5-by-5 array elements to steer the array to 5°; b) Directivity of 5-by-5 patch array antenna steered to 5° without (red) and with (blue, green, navy) phase quantization

In Fig. 10, the smaller NumBits value is, the more pronounced are discrepancies between the cases with and without quantization. As can be seen in Fig. 10a, without quantization, phase shifts of -15.688° and -31.376° are applied to the [1,2] - [5,2] and [1,3] - [5,3] elements, respectively. In contrast, when NumBits is set to 4, a uniform phase shift of -22.5° is applied to the elements [1,2] through [5,3]. This discrepancy is evident in Fig. 10b in terms of null locations in the pattern and discrepancies between the main and side lobe maximum levels, measuring 0.01 dB and 1.35 dB, respectively.

Fig. 11 shows the variation of phase shift and directivity when the 5-by-5 array is steered to 15° (Figs. 11a and 11b) and 30° (Figs. 11c and 11d). Again, the red, blue, green, and navy curves correspond to cases of no quantization and NumBits equal to 4, 5, and 6, respectively.

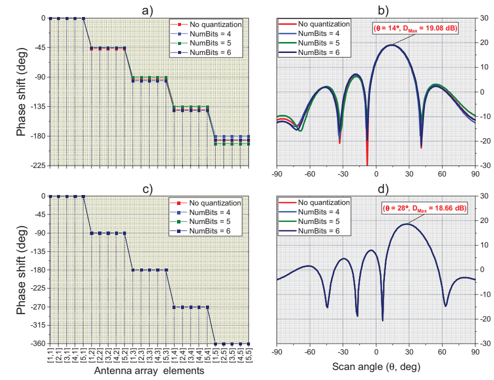

Fig. 11. a) Phase shift values without (red) and with (blue, green, navy) phase quantization for steering 5-by-5 array to 15°; b) Directivity of 5-by-5 patch array antenna steered to 15° without (red) and with (blue, green, navy) phase quantization; c) Phase shift values without (red) and with (blue, green, navy) phase quantization for steering 5-by-5 array to 30°; d) Directivity of 5-by-5 patch array antenna steered to 30° without (red) and with (blue, green, navy) phase quantization

As can be seen in Fig. 11a, achieving a 15° steering angle for the 5-by-5 array necessitates an incremental phase shift of -46.587° without phase quantization. However, when phase quantization is introduced, the smallest levels to which the phase shift values are quantized are 22.5°, 11.25°, and 5.625° for NumBits = 4, 5, and 6, respectively. As a result, when compared to the scenario depicted in Fig. 10, the disparities between the maximum levels of the main lobe and side lobes decrease. Specifically, these discrepancies are reduced to 0.009 dB and 0.29 dB, respectively, when the array is steered to a 15° angle.

According to Fig. 11c, the 5-by-5 array is steered to 30° with an incremental phase shift of -90°, which remains consistent both in the absence and presence of quantization across all three NumBits values. Consequently, directivity curves plotted in Fig. 11d are identical. The foregoing discussion leads us to conclude that the impact of phase quantization could be notable when dealing with smaller values of NumBits and decreasing steering angles. Note that because of the finite size of the 5-by-5 array and mutual coupling between its adjacent elements, the maxima of directivity for 15° and 30° steering angles occur at 14° and 28°, respectively, as indicated in Figs. 11b and 11d.

Impact of array antenna element failure on directivity

In this section we explore the impact of antenna array element failure on the performance of 5-by-5 and 16-by-16 antenna arrays. Specifically, the focus is on the main lobe directivity and its variation with element failure rate.

The antenna array failure analysis is performed using a probabilistic Monte Carlo method whereby a custom failure parameter is defined to enable or disable selected antenna elements. The length of the failure parameter is the same as the total number of antenna elements and it assumes a value of either 0 or 1, where the former signifies complete element failure (elements are unable to either radiate or receive signals), whereas the latter indicates the absence of failure (all elements are fully functional). It is assumed that random sequences of array elements are switched and off on every run of the failure analysis. Fig. 12 displays 3-D directivity plots for 5-by-5 (top) and 16-by-16 (bottom) arrays at 3 different rates of antenna element failure: 0% (Figs. 12a and 12d), 20% (Figs. 12b and 12e), and 60% (Figs. 12c and 12f).

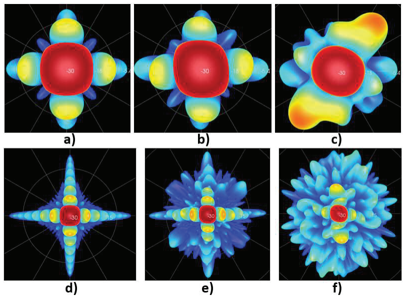

Fig. 12. Top view of directivity for 5-by-5 (top row) and 16-by-16 (bottom row) antenna arrays with 0%, 20% and 60% antenna elements failing (from left to right)

At 0% failure, we can observe well-defined and symmetric radiation patterns (a main lobe and sidelobes formed away from the main beam) resulting from coherent combination of signals from fully functional array elements. The radiation patterns start to deteriorate with increasing element failure rate. At 20% failure rate, main lobe D_{MAX} for both arrays decreases by about 2%. However, when 60% of elements fail to operate, the 5-by-5 array, being the smaller array of the two, experiences a more significant degradation in performance. Consequently, its main lobe D_{MAX} drops by about 15%. By contrast, the main lobe D_{MAX} for the 16-by-16 array decreases by about 10% from its value in the case of fully functional array elements (0% failure).

It should be noted that with 20% of elements failing, the 3-dB beamwidth for the 5-by-5 ranges from 18.9 to 20.2° with a standard deviation of 0.54°. However, at a 60% failure rate, the 3-dB beamwidth experiences a broader variation spanning from 17.5 to 21.8°, with the standard deviation being three times that observed at the 20% failure rate. In contrast, for the 16-by-16 array, the 3-dB beamwidth varies between 6.10° and 6.47°, displaying a consistently small standard deviation of 0.2° at both the 20% and 60% failure rates.

Fig. 13 shows the variation of the mean of the maximum value of main lobe directivity ($D_{MAX\ Mean}$) on a log scale with element failure percentage for 3-by-3, 5-by-5, 7-by-7, 10-by-10, 14-by-14, 16x6, and 20-by-20 arrays.

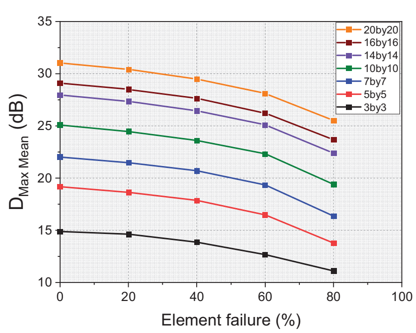

Fig. 13. $D_{MAX\ Mean}$ vs. array antenna element failure (%) for 3-by-3, 5-by-5, 7-by-7, 10-by-10, 14-by-14, 16-by-16, and 20-by-20 arrays

For each of the N-by-N arrays in Fig. 13, $D_{MAX\ Mean}$ is recorded and then averaged over 10 sample runs of the Monte Carlo analysis. As element failure varies from 0 to 80%, $D_{MAX\ Mean}$ drops by about 25%, 28%, 26%, 23%, 20%, 19%, and 18% for 3-by-3, 5-by-5, 7-by-7, 10-by-10, 14-by-14, 16-by-16, and 20-by-20 arrays, respectively. A comparison of the smallest (3-by-3) and largest (20-by-20) arrays shows that $D_{MAX\ Mean}$ for the latter is over 50% larger than that of the former over the entire failure range in Fig. 13. Except for 3-by-3, 5-by-5, and 7-by-7 arrays, $D_{MAX\ Mean}$ drop decreases with increasing N. It should be noted that all arrays are still functional when the probability of failure is as high as 80%, albeit with a significantly reduced directivity and consequently gain.

Array size and its power consumption implications

Power consumption is a key challenge in array antenna design, influencing factors like thermal and mechanical design complexity, power supply limitations, and operational costs. The array size is determined based on the required system gain (SG) and the output power of each amplifier (PA) in Fig. 6. Given a system with a known gain SG (dBm), the number of PAs required for a rectangular N-by-N array can be estimated as follows [5]:

$$M = 10^{\frac{[SG(dBm) - P_{TX}(dBm) - 2\times G(dBi)]}{30}}$$

where M is the number of active components (PAs), SG is the system gain (dBm), G is the antenna array realized gain (dBi), and P_{TX} is the output power of each PA. The equation for M assumes that each antenna element is driven by one PA. Equation is plotted in Fig. 14 for 5 rectangular arrays and a system whose gain is equal to 102 dBm [5].

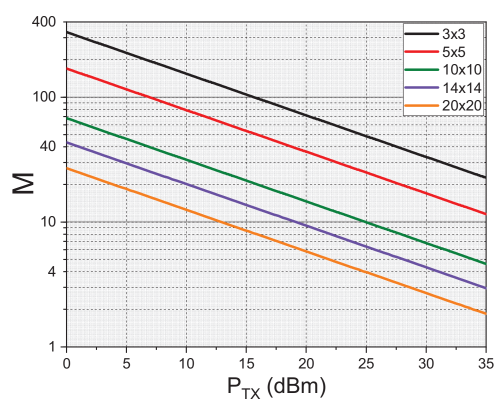

Fig. 14. Plot of M for SG = 102 dBm and 3-by-3 (red), 5-by-5 (blue), 10-by-10 (green), 14-by-14 (orange), and 20-by-20 (navy) patch antenna arrays

The values of realized gain, G, extracted from Fig. 9 and used in plotting Fig. 14 are 13.18 dBi, 17.55 dBi, 23.52 dBi, 26.44 dBi, and 29.53 dBi for 3-by-3, 5-by-5, 10-by-10, 14-by-14, and 20-by-20 arrays, respectively. It is clear from the graph that having as big an array as possible is advantageous and the lager the array, the smaller is the number of PAs required for achieving a given system gain. According to Fig. 14, the number of PAs required for the 20-by-20 patch antenna is, respectively, 6 and 12 times smaller than that required for 5-by-5 and 3-by-3 arrays over the entire P_{TX} range.

Sidelobe level reduction using Taylor Taper

In certain applications that require low sidelobe levels, several array design techniques involving Taylor, Barlett, Hamming, or Gaussian tapers can be used to control the sidelobe levels and beamwidth of phased array antennas [10]. Array pattern tapering analysis presented here is based on the Taylor window, which is enabled in the Attenuator module in Fig. 6 by specifying two parameters, NumBars and SideLobeLevel, where NumBars represents an approximate number of sidelobes that are at SideLobeLevel dB below the peak of the main lobe. The lower NumBars is, the greater is the number of sidelobes adjacent to the main lobe that are affected. In this paper, we consider the Taylor window with NumBars = 3 and SideLobeLevel = -20 dB, which is a design that is readily implemented in practice. Fig. 15 displays directivity plots for 5-by-5, 10-by-10, 16-by-16, and 20-by-20 arrays in the $\phi = 0°$ elevation plane before (red) and after (blue) using the Taylor window.

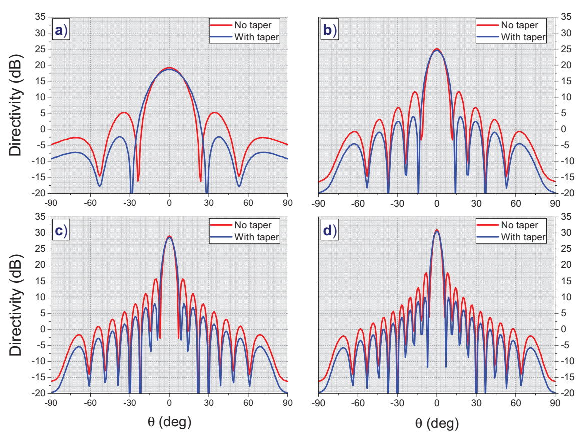

Fig. 15. Directivity vs. zenith angle, θ, in $\phi = 0°$ plane without (red) and with (blue) taper for a) 5-by-5, b) 10-by-10, c) 16-by-16, and d) 20-by-20 arrays

The application of taper has the effect of reducing the main lobe peak directivity by 2.8%, 1.8%, 1.5%, and 1.4% for 5-by-5, 10-by-10, 16-by-16, and 20-by-20 arrays, respectively. In Figs. 15a through 15d, the largest side lobes are at least 20 dB lower than the main lobe and the amount of tapering decreases progressively away from the main lobe. As can be observed, lowering the array sidelobe levels occurs at the expense of broadening the main lobe and reducing its peak directivity. This is explored in more detail next.

Figs. 16a and 16b show the variation of main lobe peak directivity (D_{MAX}) and its 3-dB beamwidth with θ for 5-by-5, 10-by-10, 16-by-16, and 20-by-20 arrays. The open circles and solid squares represent cases without and with taper, respectively.

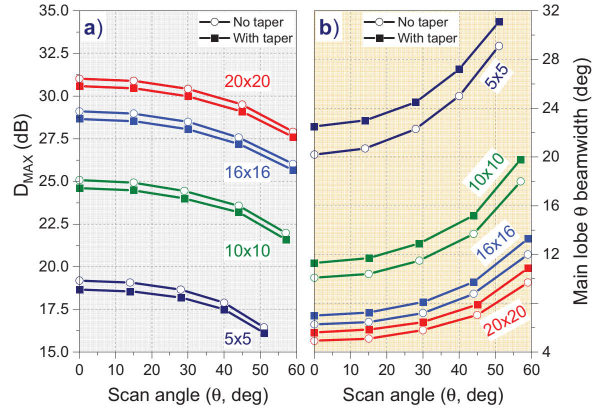

Fig. 16. a) Main lobe peak directivity (D_{MAX}) vs. zenith angle, θ, in $\phi = 0°$ plane with (solid squares) and without (open circles) taper for 5-by-5 (navy), 10-by-10 (green), 16-by-16 (blue), and 20-by-20 (red) arrays; b) Main lobe 3-dB beamwidth vs. zenith angle, θ, in $\phi = 0°$ plane with (solid squares) and without (open circles) taper for 5-by-5 (navy), 10-by-10 (green), 16-by-16 (blue), and 20-by-20 (red) arrays

In Fig. 16a, the percentage difference between D_{MAX} values without and with taper decreases with increasing scan angle and N. Specifically, the largest and smallest % differences are 2.8% and 1% and they occur at N = 5 and θ = 0° and N = 20 and θ = 59°, respectively. Applying the taper decreases D_{MAX} and the smaller the array, the more pronounced is the drop. In Fig. 16a, D_{MAX} drops by 14%, 12%, 11%, and 10% as θ ranges from 0° to 51°, 57°, 59° for 5-by-5, 10-by-10, 16-by-16, and 20-by-20 arrays, respectively.

For both cases in Fig. 16b, the % change in 3-dB beamwidth increases from about 14% to 27% with θ and as the size of the array increases from 5 to 20. Note that the change in the 3-dB beamwidth follows an opposite trend compared to D_{MAX}, as the percentage difference between the 3-dB beamwidth values without and with tapering grows with higher scan angles and larger values of N. Consequently, the % difference between 3-dB beamwidth values without taper and those with taper is approximately 6%, 9%, 10%, and 11% for 5-by-5, 10-by-10, 16-by-16, and 20-by-20 arrays, respectively. According to Fig. 16b, the worst performer among the four arrays is the 5-by-5 array whose main lobe beamwidth becomes over 2° broader when the taper is applied. By contrast, the main lobe beamwidths for the 10-by-10, 16-by-16, and 20-by-20 arrays widen by at most 1.8°, 1.3°, and 1.2°, respectively, after the taper application.

Discussion of results

The paper presents EM and system-level simulations and characterization of N-by-N phased antenna arrays at 150 GHz for 6G applications. The findings of the study reveal several key insights into N-by-N phased antenna arrays ranging in size from N = 3 to N = 20.

Firstly, as the desired scan angle increases, greater phase adjustments are required to steer the beam effectively. Array size and mutual coupling significantly impact the achievable steering range, with larger arrays offering superior performance. Smaller arrays are more susceptible to mutual coupling effects, leading to limitations in their steering capabilities. Notably, the 20-by-20 array outperforms its smaller counterparts, maintaining high directivity across a wider steering range.

Moreover, the study demonstrates that main lobe beamwidth widens as the scanning angle increases, benefiting applications requiring broader coverage. Smaller arrays, however, exhibit a more gradual increase in beamwidth, maintaining a focused beam even at higher steering angles. Additionally, the study underscores the considerable influence of phase quantization on beam steering accuracy, particularly for smaller NumBits and smaller steering angles, which has implications for applications like radar and communication systems. The impact of element failure varies with array size, with larger arrays showing greater resilience. Even at high failure rates, all arrays remain functional but with reduced performance, highlighting the importance of robust array design.

Tapering, while effective in controlling sidelobes, comes at the cost of reduced main lobe peak directivity, and the extent of this reduction varies with scan angle and array size. These findings emphasize the trade-offs between sidelobe control and main lobe characteristics, necessitating careful consideration in array design for specific applications.

Finally, when each array element is driven by a single PA, using the largest array becomes beneficial because it necessitates fewer PAs to attain a specific system gain. For instance, the analysis demonstrates that as P_{TX} varies from 0 dBm to 35 dBm, the 20-by-20 array requires approximately 6 to 12 times fewer PAs compared to the 5-by-5 and 3-by-3 arrays.

Conclusions

Currently, no comprehensive system-level modelling exists for large antenna arrays in the 110-170 GHz D-Band range. This paper presents an innovative approach that combines EM and system-level modelling techniques to analyze N-by-N phased antenna arrays with dimensions ranging from N = 3 to N = 20 at 150 GHz. This investigation is particularly directed toward high-transmit antenna arrays constructed using compact patch antennas, making them highly suitable for AoP and AiP implementations. As such, they stand out as promising contenders for future wireless 6G technologies and are currently the focal point of extensive academic research.

The reported work goes beyond the conventional scope and provides insight into the influence of failure probability, phase quantization and tapering on array directivity, gain, and beamwidth. Specifically, it is shown that the impact of quantization is influenced by both the number of quantization bits and the steering angle, with smaller bit counts and smaller angles leading to more noticeable deviations from ideal beam patterns. Also, larger arrays, e.g., 16-by-16, perform better when some elements fail compared to smaller arrays like 5-by-5 due to redundancy, which is crucial for reliability in critical applications. Moreover, tapering reduces main lobe peak directivity, especially in smaller arrays. The 3-dB beamwidth widens with taper, more so in larger arrays and steering angles. Trade-offs between sidelobe control and main lobe traits highlight the need for careful consideration based on application needs.

References

1. Maiwald, T., Li, T., Hotopan, George-R., Kolb, K., Disch, K., Potschka, J., Haag, A., Dietz, M., Debaillie, B., Zwick, T., Aufinger, K., Ferling, D., Weigel, R., and Visweswaran, A., "A Review of Integrated Systems and Components for 6G Wireless Communication in the D-Band," *Proceedings of the IEEE*, Vol. 111, No. 3, March 2023, pp. 220-256.
2. Zheng, Kai B., Sun, M., Guo, Yong X., "Wideband Circularly Polarized FOWLP Antenna in Package for Satellite Communications," *IEEE 73nd Electronic Components and Technology Conference (ECTC)*, 2023, pp. 2166-2171.
3. Farid, Ali A., Ahmed, Ahmed S. H., Simsek, A., Rodwell, Mark J. W., "A Packaged 135GHz 22nm FD-SOI Transmitter on an LTCC Carrier," *IEEE/MTT-S International Microwave Symposium*, 2021, pp. 713-716.
4. Jia, X., Li, X., Moon, Kyoung-s., Kim, Joon W., Huang, Kai-Q., Jordan, Matthew B., and Swaminathan, M., "Antenna-Integrated, Die-Embedded Glass Package for 6G Wireless Applications," *IEEE 72nd Electronic Components and Technology Conference (ECTC)*, 2022, pp. 377-383.
5. Caicedo Mejillones, S., Oldoni, M., Moscato, S., Fonte, A., and D'Amico, M., "Power Consumption and Radiation Trade-offs in Phased Arrays for 5G Wireless Transport," *43rd International Conference on Telecommunications and Signal Processing (TSP)*, Milan, Italy, July 2020, pp. 112-116.
6. Huang, Kai-Q., Swaminathan, M., "Antennas in Glass Interposer For sub-THz Applications," *IEEE 71st Electronic Components and Technology Conference (ECTC)*, 2021, pp. 1150-1157.
7. Gu, X., Liu, D., and Sadhu B., "Packaging and Antenna Integration for Silicon-Based Millimeter-Wave Phased Arrays: 5G and Beyond," *IEEE Journal of Microwaves*, Vol. 1, No. 1 (2021), pp.123-134.
8. Le, Thi H., Schwanitz, O., Ndip, I., Mueller, F., Braun, T., Schneider-Ramelow, M., "Design, Fabrication and Measurement of FOWLP-based Series-Fed Antennas for 6G D-Band MIMO Applications," *IEEE 9th Electronics System-Integration Technology Conference (ESTC)*, 2022, pp. 593-596.
9. Balanis, C. A., Antenna Theory Analysis and Design, John Wiley & Sons, Inc. (Hoboken, New Jersey, 2016), pp. 788-792.
10. Fenn, Alan J., Electromagnetics and Antenna Technology, Artech House (Boston/London, 2018), pp. 163-169.